Integration of Eight-Channel Directly Modulated Membrane-Laser Array and SiN AWG Multiplexer on Si

Hidetaka Nishi, *Member, OSA*, Takuro Fuji, *Member, IEEE*, Nikolaos-Panteleimon Diamantopoulos, *Member, OSA*, Koji Takeda, *Senior Member, IEEE*, Erina Kanno, Takaaki Kakitsuka, *Member, IEEE*, Tai Tsuchizawa, Hiroshi Fukuda, *Member, IEEE*, and Shinji Matsuo, *Fellow, IEEE*

(Top-Scored Paper)

***Abstract*—Eight-channel 56-Gbit/s direct four-level pulse-amplitude modulation is demonstrated using a 1.3-μm wavelength-division-multiplexing (WDM) photonic integrated circuit (PIC) transmitter, consisting of membrane distributed-reflector lasers heterogeneously fabricated on Si and a SiN arrayed-waveguide-grating multiplexer. Direct bonding, epitaxial regrowth, and low-temperature SiN-waveguide fabrication technologies are employed for the integration on Si. Using a nonlinear equalizer, we operated the fabricated WDM PIC transmitter with a low power consumption of 403 fJ/bit for overall 448 Gbit/s signals. The total eight-channel bit-error rate was 2.7 $\times$ 10^{-3}, which is less than the 7%-overhead hard-decision forward-error-correction limit.**

***Index Terms*—Arrayed-waveguide grating multiplexer, direct bonding, heterogeneous integration, semiconductor lasers, SiN waveguide, wavelength division multiplexing.**

I. Introduction

SUPPORTING the continuous growth of data traffic for short- to middle-reach optical interconnections over 400 Gbit/s will require low-power-consumption and low-cost wavelength division multiplexing (WDM) transmitters. In this context, the use of directly modulated lasers (DMLs) is a promising solution and long-wavelength vertical-cavity surface emitting lasers (VCSELs) have attracted much attention [1]–[3]. However, there are still some challenges related to precise wavelength control of VCSELs and fabrication of WDM modules including multiplexing optics. In particular, in-plane lasers, such as distributed-feedback (DFB) lasers, are considered to have good compatibility with the WDM configuration, thanks to the controllability of their wavelength using a grating. Nonetheless, the power consumption and cost of in-plane lasers are rather high.

Introduction of Si photonics technology is regarded as a breakthrough in laser implementation, and there have been many studies on, e.g., III-V/Si hybrid or monolithic approaches [4]–[6], to fabricating DFB lasers on large-scale Si substrates. In addition, WDM transmitter PICs on Si have also been reported [7]–[9]. However, most of them consist of external modulators and on- or off-chip continuous-wave light sources, which mean issues still remain regarding the power consumption.

To overcome these problems, we have proposed and demonstrated directly modulated membrane buried heterostrucure (BH) lasers on Si [10]–[13]. Employing BH and a thin membrane structure on a SiO_2 layer provides good carrier and optical confinements in the active region, which helps to reduce power consumption. Moreover, the membrane lasers are heterogeneously fabricated on a Si substrate by combining O_2-plasma assisted direct bonding technology and buried regrowth on InP/SiO_2/Si substrate, which enables manufacture of in-plane lasers on large-scale Si substrate. Overall, this is a promising way to manufacture photonic integrated circuits.

II. Device Structure and Fabrication Process

First, we briefly introduce the device configuration in the WDM transmitter PIC. Fig. 1 shows a top view of the integrated PIC, which has an overall footprint of 1.8 $\times$ 2.0 mm^2. The eight-channel membrane distributed-reflector (DR) laser [11], [12] array has a 250-μm channel separation. The output signal from each membrane DR laser is coupled to an InP waveguide with a SiO_2 cladding, which has about 40% refractive-index contrast (Δ). The InP waveguide is connected to a 20%-Δ SiN waveguide via the InP-SiN SSC. The eight-wavelength inputs from the SiN waveguides are connected to the SiN AWG multiplexer. After passing through the AWG, the eight-wavelength signals are multiplexed and output from the SiN waveguide. The design and device structure of all the integrated components are described in detail in the following sub-sections. The integration process of for these components is also explained.

Manuscript received July 1, 2018; revised August 17, 2018; accepted September 4, 2018. Date of publication November 13, 2018; date of current version February 20, 2019. *(Corresponding author: Hidetaka Nishi.)*

The authors are with the NTT Device Technology Laboratories, NTT Corporation, Atsugi-shi 243-0198, Japan (e-mail: hidetaka.nishi.sf@hco.ntt.co.jp; fujii.takuro@lab.ntt.co.jp; diamantopoulos.np@lab.ntt.co.jp; takeda.koji@lab.ntt.co.jp; kanno.erina@lab.ntt.co.jp; kakitsuka.takaaki@lab.ntt.co.jp; tsuchizawa.tai@lab.ntt.co.jp; fukuda.hiroshi@lab.ntt.co.jp; matsuo.shinji@lab.ntt.co.jp).

Color versions of one or more of the figures in this paper are available online at http://ieeexplore.ieee.org.

Digital Object Identifier 10.1109/JLT.2018.2873742

This work is licensed under a Creative Commons Attribution 3.0 License. For more information, see http://creativecommons.org/licenses/by/3.0/

Fig. 1. Top view of an AWG-DML integrated PIC.

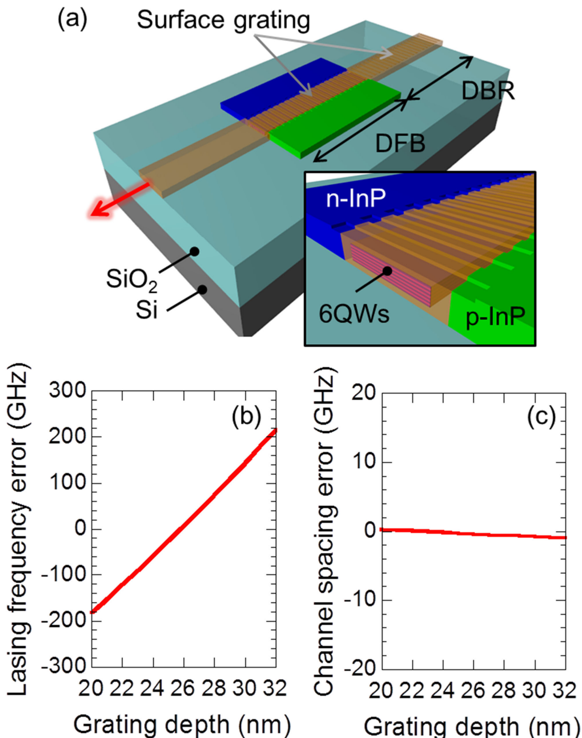

Fig. 2. (a) Schematic device structure of the membrane DR laser. The inset shows a schematic cross-sectional image of the DFB laser part. (b) and (c) calculated lasing frequency error and channel spacing error as a function of grating depth.

A. *Membrane DR Laser*

Fig. 2(a) shows a schematic diagram of the device structure of the membrane DR laser, which can be directly modulated by lateral current injection. The device structure is quite similar to the ones previously reported by our group [10]–[13]. The large refractive index difference between the InP and SiO_2 provides a higher optical confinement factor (Γ) than that of conventional on-InP lasers, which leads to a high modulation current efficiency factor and low power consumption [10]–[13]. The membrane DR laser consists of an 80-μm-long DFB laser part and a 40-μm-long back-side distributed-Bragg-reflector (DBR) part. The gain medium of the DFB laser consists of six InGaAsP-based quantum wells (QWs), which are embedded in a 280-nm-thick InP slab. To make a lateral current injection structure on the DFB laser part, p- and n-InP regions are formed on both sides of the six QWs. The DBR consists of an InP waveguide. Both the DFB and DBR surface gratings are formed on top of the InP layer by etched InP covered with SiO_2. To achieve low operation energy and high output power at the same time, the coupling coefficient (κ) of the gratings is designed to be as high as 600 cm^{-1}. To suppress spatial hole burning while managing such a high-κ DFB cavity, we used uniform-pitch gratings instead of a λ/4-shift design. Stable single-mode lasing can be obtained by selecting a single mode from the DFB-cavity stop-band edges using a DBR mirror, with a one-sided optical output provided from the front-side InP waveguide. To accommodate eight-wavelength lasing channels, the designed Bragg wavelengths of the DFB and DBR gratings are shifted accordingly for each channel.

For integrating the AWG multiplexer, its passband have to be matched to the lasing wavelength. Here, we discuss how finely the lasing wavelength can be controlled on the membrane DR laser. Because of the strong optical confinement and high κ, the lasing wavelength of the membrane DR laser is thought to be sensitive to fabrication error. In particular, the fabrication error of the grating structure seems to be the dominant cause of wavelength variation compared with other considerable contributions, such as errors in the refractive index and thickness of the InP-based crystals grown by metal-organic vapor phase epitaxy (MOVPE). Fig. 2(b) shows the results of a calculation evaluating how sensitive the lasing wavelength is to the fabrication error of the grating depth. In particular, the designed lasing wavelength is obtained with a grating depth of 26 nm. When a grating-depth error of $\pm$5 nm occurs, the lasing wavelength error is estimated to be less than $\pm$200 GHz, which is compatible with the 400GBASE-FR8/LR8 WDM channel assignment [14]. Compared with the lasing wavelengths, the channel spacing is easier to maintain. Fig. 2(c) shows the calculated relationship between the channel spacing and grating depth. When a grating-depth error of $\pm$5 nm occurs around the designed depth of 26 nm, the channel spacing error is less than $\pm$1 GHz. Thus, when fabrication errors occur, the eight lasing wavelengths tend to shift, but the channel spacing remains almost the same. Note that when the membrane DR laser is operated, the lasing wavelength can be varied by using bias current in combination with temperature control, which can be utilized for fine tuning of the wavelength.

B. *InP-SiN Spot-Size Converter*

At the interface between the membrane DR laser and the InP waveguide, the InP core width narrows from 1.5 to 0.1 μm at its end by using a linear taper with a length of 200 μm and constant InP core height of 280 nm. Besides that, a single-mode SiN waveguide core, with cross-sectional dimensions of

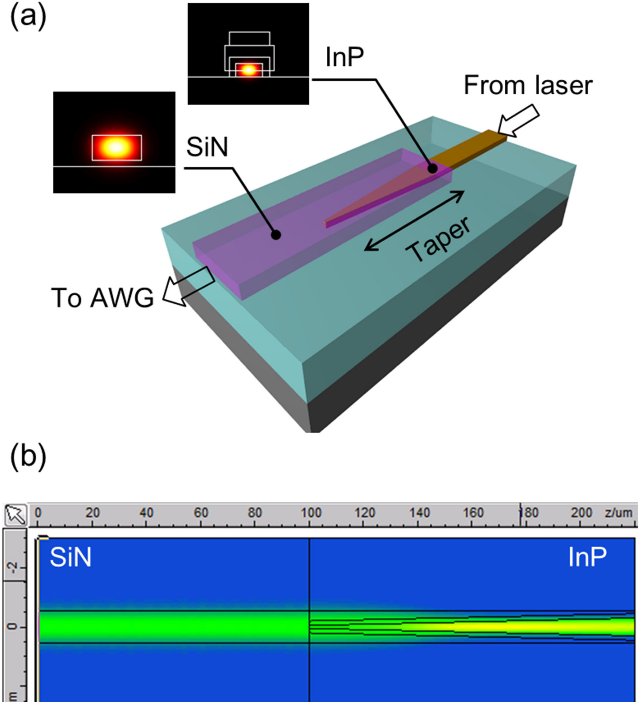

Fig. 3. (a) Schematic birds-eye view of the InP-SiN SSC and mode fields at each indicated position. (b) Top view of calculated 1310-nm lightwave intensity propagating in the InP-SiN SSC.

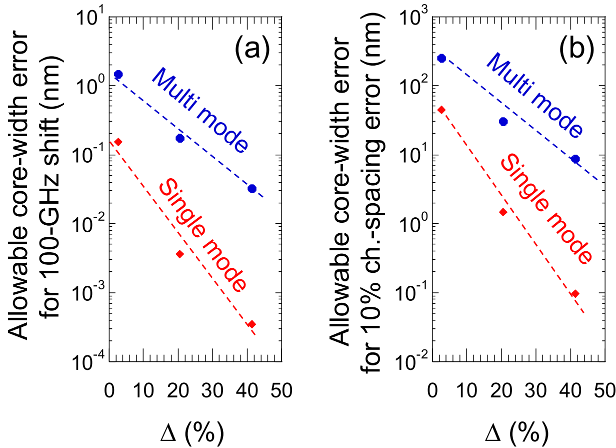

Fig. 4. (a) Calculated relationship between Δ and the allowable core-width error to achieve 100-GHz λ_0 shift. (b) Calculated relationship between Δ and the allowable core-width error to obtain AWG channel-spacing error of less than 10%.

450 × 900 nm, is placed above the InP taper. This structure enables us to achieve low-loss adiabatic mode conversion while compensating for the large Δ difference from the InP to the SiN waveguide according to the conventional principle [15]. Note that stacked Si-InP waveguide couplings with similar effective indexes have already been achieved by using a taper structure [16]–[18]. Because the DFB and DBR gratings are ethed InP covered with SiO_2, the InP core is also covered with SiO_2, This means the SiO_2 layer exists between the InP and SiN cores.

Fig. 3(a) shows a schematic birds-eye view of the InP-SiN SSC and calculated mode fields at the InP waveguide and the SiN waveguide. Fig. 3(b) shows a top view of the calculated intensity of the 1310-nm lightwave propagating through the SSC. Here, we used the eigenmode expansion method. The transmission loss is estimated to be 0.2 dB.

C. 1.3-μm SiN Waveguide and AWG Multiplexer

To achieve a small AWG multiplexer footprint while maintaining high input power and good fabrication-error tolerance, we used a SiN waveguide for its moderately high Δ compared to that of an InP waveguide. We have already reported a SiN waveguide at 1310 nm with a propagation loss of 1.0 dB/cm [19].

Actually, the Δ of the InP waveguide is as high as that of the Si waveguide, which can help to reduce the device footprint. However, it may cause serious issues when there is a WDM multiplexer on the transmitter PIC. Under the assumption of a 5-mW output from each membrane DR laser, a 40-mW multiplexed signal is confined in a single output waveguide core on the eight-channel WDM transmitter PIC. When the lightwave with this power propagates in the InP waveguide, non-negligible nonlinear effects, such as two-photon absorption (TPA) and four-wave mixing, occur, which leads to additional loss and wavelength conversion. Note that the InP waveguide has a higher nonlinear index (n_2) and TPA coefficient (β) than those of the Si waveguide at around 1550 nm [20]. Another concern is fabrication-error tolerance as it relates to the performance of the AWG multiplexer. The higher Δ requires precise fabrication of the core dimensions. A key requirement is that the AWG passband has to be aligned to the lasing wavelength even if fabrication errors exist. Here, let us consider how the center wavelength (λ_0) of the AWG passbands with the same grating order (M) varies depending on the variation in the core width of the arrayed waveguide (w_{aw}). From the well-known AWG multiplexer principle, $\partial\lambda_0/\partial w_{\mathrm{aw}}$ can be expressed as

$$\frac{\partial \lambda_0}{\partial w_{\mathrm{aw}}} = \frac{\partial n_{\mathrm{eff}}}{\partial w_{\mathrm{aw}}} \frac{\Delta L}{M}. \tag{1}$$

Here, n_{eff} is the effective refractive index of the arrayed waveguide, and ΔL is the propagation length difference between adjacent array waveguides. Fig. 4(a) shows the calculated relationship between Δ and the allowable core-width error to obtain a λ_0 shift of less than 100 GHz. When we use a single-mode waveguide for the array, the allowable core-width error is 0.15 nm for a SiO_xN_y waveguide ($\Delta = \sim 3\%$), 4×10^{-3} nm for a SiN ($\Delta = \sim 20\%$) waveguide, and 4×10^{-4} nm for a Si and InP ($\Delta = \sim 40\%$) waveguide, respectively. These values are impractical from the viewpoint of fabrication. To make fabrication easier, the use of a multi-mode waveguide is helpful [21]. Fig. 4(a) shows the relationship for the arrayed waveguide with a four times wider core. As shown, this approach mitigates the allowable error to 0.17 nm for the SiN waveguide, but even so, this value is still unpractical. Thus, we must accept the AWG-passband shift due to the fabrication error.

To deal with this shift and still achieve matching between the lasing wavelength and the AWG passband, we introduce a cyclic channel configuration that enables us to choose the nearest AWG passband from the lasing wavelength by controlling the membrane-DR-laser bias current. The key AWG specification

for doing so is the channel spacing of the filter passband. Here, let us consider how the channel spacing of the AWG passband ($\Delta\lambda$) varies depending on the error of w_{aw}. $\partial\Delta\lambda/\partial w_{\mathrm{aw}}$ can be expressed as

$$\frac{\partial\Delta\lambda}{\partial w_{\mathrm{aw}}} = \frac{\partial\left(n_{\mathrm{eff}}/n_g\right)}{\partial w_{\mathrm{aw}}}\frac{n_{\mathrm{slab}}}{M}\frac{p_{\mathrm{IO}}\ p_{\mathrm{array}}}{R_{\mathrm{slab}}}\,. \tag{2}$$

In this equation, n_{g} is the group index of the arrayed waveguide, n_{slab} is the index of the slab, p_{IO} is the separation pitch between cores connected to the slab for the AWG input and output, p_{array} is the separation pitch between cores connected to the slab for the arrayed waveguides, and R_{slab} is the radius of the slab. Fig. 4(b) shows the relationship between Δ and the allowable core-width error to achieve a variation of less than 10% in $\Delta\lambda$. To make a single-mode InP waveguide with a Δ of $\sim$40%, the error must be less than 0.1 nm and the uniformity must be good in the longitudinal direction; again, this is impractical. Clearly, as Δ decreases, the allowable core-width error increases and the fabrication difficulty decreases. Although the use of a single-mode waveguide requires a severe core-width control, the use of a multimode waveguide mitigates allowable error for the SiN waveguide to 30 nm.

Actually, a larger w_{aw} leads to more propagation modes, which makes it difficult to maintain the fundamental mode propagation that keeps the interferometric process in the AWG multiplexer simple. To avoid higher mode propagation as much as possible, the multimode waveguide should be configured only in the straight part, and the single-mode one must be used in the bending part [21]. These different waveguides are connected with a linear taper. For the other normal wiring in the AWG multiplexer, the SiN core width is set to 900 nm. The thickness of SiN core is set to 450 nm. The number of arrayed waveguides in the AWG multiplexer is 40, and the free-spectrum range (FSR) is designed to be 3040 GHz (=8 channels $\times$ 380 GHz) for the cyclic configuration. "Free-space" star couplers without sidewall definition of slab waveguide cores are placed at the arrayed-waveguide input and output [21]. The width of the SiN core at the chip facet on the output side is enlarged to 3.0 μm for lensed-fiber coupling. The footprint of the AWG is 1 $\times$ 2 mm^2.

D. Fabrication Process

The fabrication process was as follows. The first step was heterogeneous fabrication of the membrane DR laser in a similar way as in our previous reports [10]–[13]. 150-nm-thick InGaAsP-based six-quantum-well layers sandwiched by top and bottom InP layers (total thickness was 280 nm) and a sacrificial layer were grown on a 2-inch InP substrate by using MOCVD technology. Then, the epitaxial layers were directly bonded to a 2-inch Si substrate with a surface SiO_2 thickness of 2 μm. After removing the InP support substrate and the sacrificial layer, the active region was buried with an InP layer to form a BH. The lateral p-i-n structure was then fabricated by ion implantation and thermal diffusion. Next, the DFB and DBR surface gratings were formed by electron-beam (EB) lithography and dry etching of the top InP surface. After that, the InP waveguide and the slab for the membrane DR laser were defined, including the DFB and the DBR region, by i-line lithography. In particular, the double-step patterning method was used for forming the InP taper of the SSC. Next, the InP layer was removed by dry etching to expose the surface SiO_2 of the substrate for fabrication of the SiN AWG multiplexer. Then, a 450-nm-thick SiN film was deposited at a temperature of less than 200 °C by electron-cyclotron-resonance (ECR) plasma-enhanced chemical vapor deposition (PECVD) with a source of a SiD_4 and N_2 gas mixture, which avoided any thermal damage to the fabricated lasers [22]. Next, the SiN waveguide and AWG multiplexer were formed by i-line lithography and reactive-ion etching. The SiO_2 overcladding was then deposited by tetraethyl orthosilicate (TEOS) PECVD. Finally, the SiO_2 above the electrode pads was removed to form the probing window, followed by blade dicing to obtain edge-coupling chip facets.

III. Device Characteristics

A. Optical Characteristics of the SiN AWG Multiplexer

First, we evaluated the passive characteristics of a SiN AWG multiplexer fabricated on SiO_2/Si substrate without the membrane DR laser integration processes. We used a praseodymium-doped fiber amplifier (PDFA) as an amplified spontaneous emission (ASE) lightsource. A transverse-electric (TE) –mode lightwave fixed by a polarization controller was fed into the SiN AWG multiplexer through a lensed fiber. The output light was also captured by the lensed fiber, which was connected to an optical spectrum analyzer. The fabricated chip was mounted on a temperature-controlled stage kept at 25 °C.

Fig. 5(a) shows the measured spectra. Here the transmittance was normalized by that of an on-chip reference waveguide. We estimated that the on-chip loss of the SiN AWG was as low as 2.3 and 4.4 dB at the center and edge channel, respectively. The interchannel crosstalk was -18 dB or more, which can be decreased by improving the design and fabrication process [21]. Fig. 5(b) shows the relationship between the channel number and the obtained center wavelength. From the slope, we evaluated the channel spacing to be 367.5 GHz, which corresponded to a 3.3% deviation from the designed channel spacing of 380 GHz. These results confirmed that our approach to designing the arrayed waveguide worked well and mitigated the fabrication error of the SiN waveguide. In addition, the average FSR in the eight channels was 3048.7 GHz, which was almost the same as the designed value.

B. Static Characteristics of the Fabricated PIC

Next, we evaluated the static characteristics of the integrated PIC. Here, to drive all eight membrane DR lasers simultaneously, we used an eight-channel direct-current (DC) multi-probe. At the output facet, a lensed fiber was aligned to a single AWG output channel. Fig. 6(a) shows the spectrum measured at a chip-stage temperature of 25 °C. It indicates stable single-mode lasing for all eight channels with 380-GHz spacing. The inset shows spectra measured at various injected currents from 0.5 to 10.0 mA. The peak output power changes as the injected current increases; this means the output signal was filtered (mul-

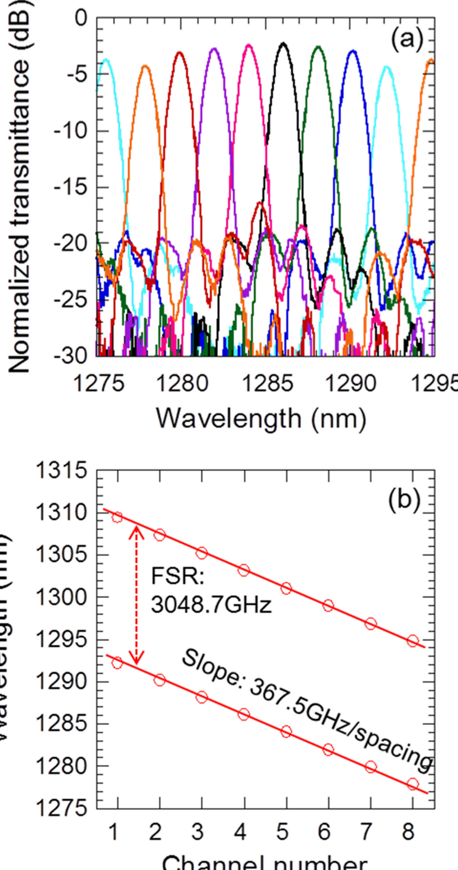

Fig. 5. (a) Transmittance spectra of the SiN AWG fabricated on a SiO_2/Si wafer without the membrane DR lasers. (b) Evaluated peak wavelength of each AWG channel.

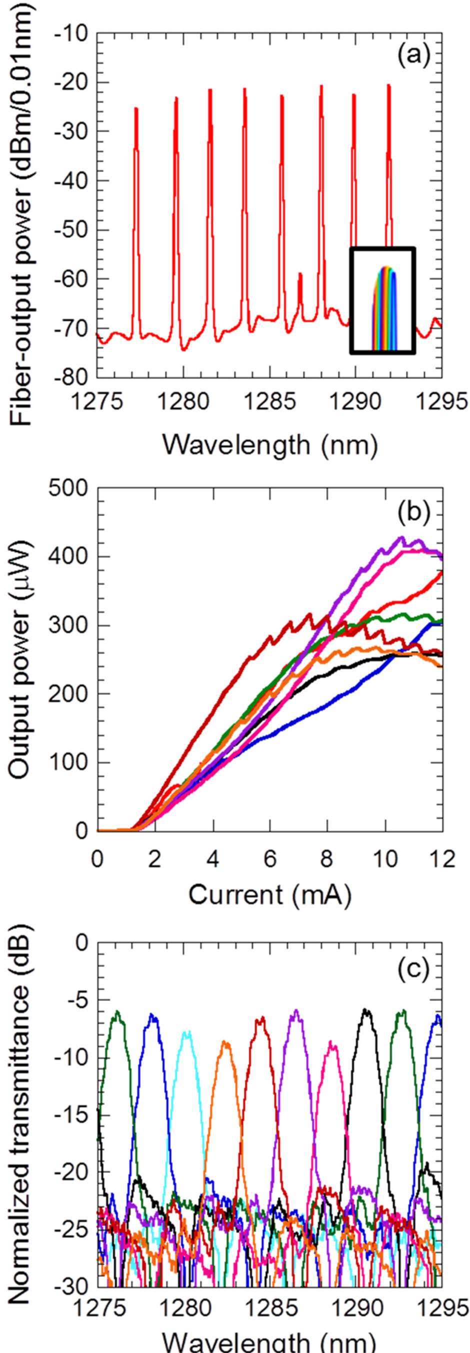

Fig. 6. (a) Spectrum obtained from fabricated PIC. (b) I-L relationships for all eight channels. (c) Transmittance spectra of integrated SiN AWG, measured after removal of the SSC and laser parts from the PIC.

tiplexed) by the integrated SiN AWG. Fig. 6(b) shows the relationship between injected current and output power (I-L) for all eight channels. The threshold currents for all channels were 1.4 ± 0.1 mA, which is quite a small variation and similar to those in previous work [11].

We estimated that the total loss for all the passive components, including the InP-SiN SSC and the SiN AWG multiplexer, and fiber coupling, was about 20 dB. Among the individual losses, the fiber coupling loss was previously evaluated to be 2.0 dB [19]. To evaluate the loss of the integrated SiN AWG multiplexer, we cut the SSC and laser parts off the PIC chip and measured the transmittance of only the AWG part. Fig. 6(c) shows the measured spectra of the integrated SiN AWG multiplexer, where the transmittance is normalized by that of an on-chip reference waveguide. We estimated that the on-chip loss of the SiN AWG varies from 5.8 to 8.8 dB. By comparing these results with the spectra in Fig. 5(a), it becomes clear that the integration increased the on-chip loss of the SiN AWG to $3.5 \sim 4.4$ dB. We suppose that this is mainly due to imperfections in the fabrication process. For example, the wafer warpage occurring before the SiN waveguide is fabricated may be different from that of a wafer without laser integration; this would lead to imperfections in the lithography and dry etching processes used to make the SiN waveguide. In addition, as we described above, the SiN waveguide was fabricated on the exposed SiO_2 layer after the bonded InP had been removed. Thus, the smoothness of the SiO_2 surface just before the AWG fabrication was worse than that of the thermally oxidized SiO_2 on a polished Si substrate. These issues can be handled by introducing additional fabrication processes, such as warpage correction and chemical-mechanical polishing, just before the SiN AWG fabrication. The remaining origin of considerable loss was the InP-SiN SSC. Instead of the ideal case of the designed

0.2-dB loss, the InP-SiN SSC seems to have a significant loss of roughly 10 dB. We consider the main reason to be lithography imperfections in the InP taper. In this study, to form the InP taper with a tip width of 100 nm, we used double (side-by-side) lithography with an i-line stepper that had non-negligible misalignment of the stage position at exposure, which leads to significant loss at the SSC. In our previous work, we used EB lithography to form a fine taper shape and experimentally confirmed a 0.4-dB loss for an InP-SiOx waveguide [15]. Thus, we expect that the InP-SiN SSC loss can be decreased to a similar value.

C. Dynamic Performance of the Fabricated PIC

Next, we demonstrated high-speed direct 8 × 56-Gbit/s PAM-4 operation of integrated DR membrane lasers that had a 3-dB bandwidth of about 20 GHz, which is enough to achieve 28-GBaud modulation [23]. Fig. 7(a) shows the experimental configuration. A 28-Gbaud Gray-encoded PAM-4 electrical signal using a 215-length pseudo-random bit sequence (PRBS) was generated by an arbitrary waveform generator with a 25-GHz analog 3-dB bandwidth and then amplified by a linear radio-frequency (RF) amplifier. The RF signal combined with a DC bias current from a bias tee was supplied to the membrane DR lasers by an RF probe. Using this configuration, we measured each channel individually. We set the DC bias current to 5.1 ∼ 18.3 mA depending on the channel under test to compensate for the mismatch between the lasing wavelength and AWG multiplexer passband. The AWG output channel was fixed during the measurements. At the receiver side, the optical signal was fed to a PDFA, filtered by a tunable optical band-pass filter (TBPF), and converted into an electrical signal by a commercial p-i-n photodiode (PD) with a 3-dB bandwidth of over 30 GHz integrated with a trans-impedance amplifier (TIA). The electrical data were stored in a digital storage oscilloscope (DSO) at a sampling rate of 80 GSa/s and processed offline to obtain eye diagrams after equalization. In this integrated device, the received signal was distorted by the mixed linear and nonlinear characteristics of the directly modulated membrane DR laser's response and the pass-band shape of the integrated SiN AWG multiplexer. To compensate for these distortions, we used a T/2-spaced, second-order polynomial nonlinear equalizer [24], [25] with memory lengths of 40 samples for the linear part and 50 samples for the nonlinear part.

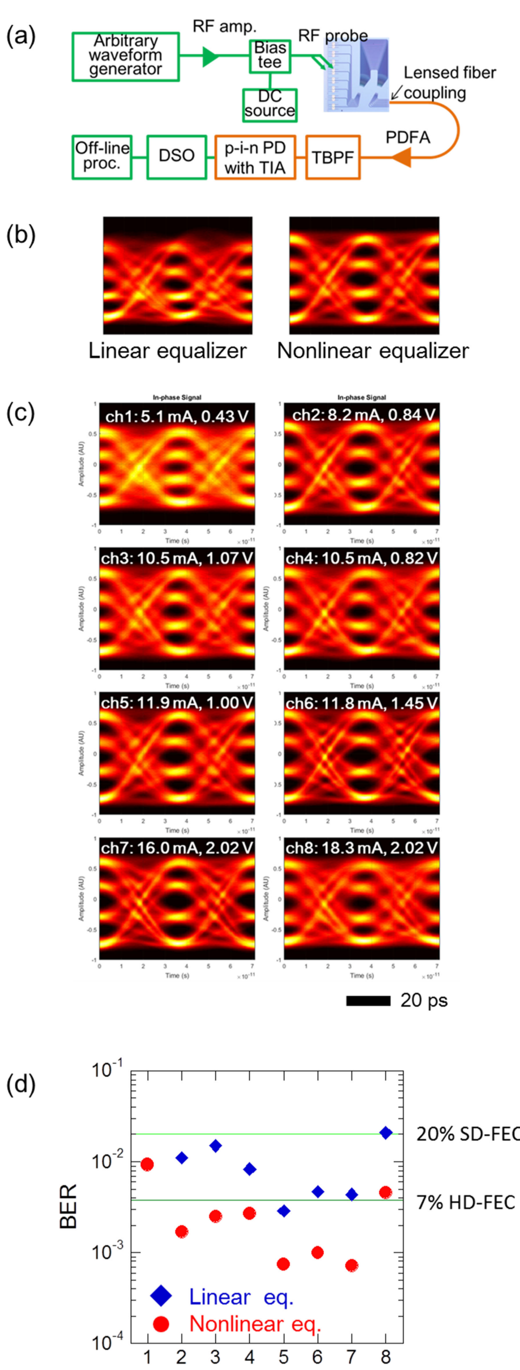

Fig. 7. (a) Experimental setup for direct modulation and BER measurement. (b) Eye diagrams after linear and nonlinear equalization for channel 7. (c) All eight eye diagram obtained with nonlinear equalizer. (d) Evaluated BER for all eight channels with a linear and nonlinear equalizer.

Fig. 7(b) shows the eye diagrams after equalization for channel 7 using only the linear part and with both linear and nonlinear terms. Clearly, the inclusion of the nonlinear (second-order polynomial) term improved the eye openings, as was previously reported for PAM with a DML [26]. Fig. 7(c) shows the obtained eye diagrams after the offline processing with the nonlinear equalizer. The DC bias current and swing voltage on each channel are indicated above each eye diagram. To draw the eye diagrams, the vertical axes were normalized so that the 00 and 11 signal levels would be consistent for all channels even though the received signal intensity varied depending on the channel. We confirmed clear eye openings at all eight channels for directly modulated optical signals after multiplexing with the integrated SiN AWG multiplexer. The total power consumption of the entire 400-Gbit/s WDM transmitter was determined to be 403 fJ/bit from the L-I-V characteristics of the laser. The estimated bit-error rate (BER) in each channel is shown in Fig. 7(d) for both linear (blue diamonds) and nonlinear (red dots) equalization. Note that we could not evaluate the BER at channel 1 with the linear equalization. Under the assumption of a combined 1 × 400G forward-error correction (FEC) architecture

for all eight channels [27], the total BER of our transmitter was 2.7×10^{-3}, which is below the 7% overhead hard-decision FEC (HD-FEC) limit of 3.8×10^{-3}. When we did not apply the nonlinear equalizer, the total BER was 9.6×10^{-3}, which is below the 20% overhead soft-decision FEC (SD-FEC) limit of 1.25×10^{-2} considered for 400-Gbit/s operation by OIF [27], [28]. We expect that increasing the fiber output power by improving the loss characteristics in the PIC will reduce the BER.

IV. Conclusion

We demonstrated the first integration of directly modulated membrane DR lasers and a SiN AWG multiplexer based on direct bonding, buried regrowth, and low-temperature SiN-waveguide fabrication technologies on Si substrate. The fabricated device exhibits direct 8 × 56-Gbit/s PAM-4 operation with a power consumption as low as 403 fJ/bit, which shows its potential for an over 400-Gbit/s WDM transmitter PIC.

Acknowledgment

The authors would like to thank Mr. Ishibashi, Mr. Shouji, Mr. Yokoyama, Ms. Sato, and Mr. Horie for their great help with the device fabrication. The authors would also like to thank Dr. Yoshimatsu, Dr. Nakanishi, Dr. Kanazawa, Dr. Tsunashima (NTT Device Innovation Center), Dr. Hasebe, and Dr. Yamazaki (NTT Device Technology Laboratories) for their valuable suggestions and fruitful discussions.

References

[1] F. Karinou *et al.*, "1.55-μm long-wavelength VCSEL-based optical interconnects for short-reach networks," *J. Lightw. Technol.*, vol. 34, no. 12, pp. 2897–2904, Jun. 2015.

[2] N. Eiselt *et al.*, "Experimental demonstration of 84 Gbit/s PAM-4 over up to 1.6 km SSMF using a 20-GHz VCSEL at 1525 nm," *J. Lightw. Technol.*, vol. 35, no. 8, pp. 1342–1349, Apr. 2017.

[3] P. Wölf *et al.*, "Spectral efficiency and energy efficiency of pulse-amplitude modulation using 1.3 μm wafer-fusion VCSELs for optical interconnects," *ACS Photon.*, vol. 4, no. 8, pp. 2018–2024, 2017.

[4] A. Abbasi *et al.*, "Direct and electroabsorption modulation of a III-V-on-silicon DFB laser at 56 Gb/s," *IEEE J. Sel. Topics Quantum Electron.*, vol. 23, no. 6, Nov./Dec. 2017, Art. no. 1501307.

[5] G. De Valicourt *et al.*, "Photonic integrated circuit based on hybrid III–V/silicon integration," *J. Lightw. Technol.*, vol. 36, no. 2, pp. 265–273, Jan. 2018.

[6] D. Inoue *et al.*, "Directly modulated 13 μm quantum dot lasers epitaxially grown on silicon," *Opt. Express*, vol. 26, no. 6, pp. 7022–7033, 2018.

[7] C. Zhang *et al.*, "8 × 8 × 40 Gbps fully integrated silicon photonic network on chip," *Optica*, vol. 3, no. 7, pp. 785–786, 2016.

[8] K. Chen *et al.*, "Wavelength-multiplexed duplex transceiver based on III-V/Si hybrid integration for off-chip and on-chip optical interconnects," *IEEE Photon. J.*, vol. 8, no. 1, Feb. 2016, Art. no. 7900910.

[9] L. Chen *et al.*, "Monolithic silicon chip with 10 modulator channels at 25 Gbps and 100-GHz spacing," *Opt. Express*, vol. 19, no. 26, pp. B946–B951, 2011.

[10] S. Matsuo *et al.*, "Directly modulated buried heterostructure DFB laser on SiO2/Si substrate fabricated by regrowth of InP using bonded active layer," *Opt. Express*, vol. 22, no. 10, pp. 12139–12147, 2014.

[11] Fujii *et al.*, "1.3-μm directly modulated membrane laser array employing epitaxial growth of InGaAlAs MQW on InP/SiO2/Si substrate," in *Proc. ECOC, Dusseldorf*, 2016, paper Th3A2.

[12] H. Nishi *et al.*, "Membrane distributed-reflector laser integrated with SiOx-based spot-size converter on Si substrate," *Opt. Express*, vol. 24, no. 16, pp. 18346–18352, 2016.

[13] T. Fujii *et al.*, "Heterogeneously integrated membrane lasers on Si substrate for low-operating energy optical links," *IEEE J. Sel. Topics Quantum Electron.*, vol. 24, no. 1, Jan./Feb. 2017, Art. no. 15004081.

[14] IEEE 802.3bs Ethernet Task Force, 2017. [Online]. Available: http://www.ieee802.org/3/bs/

[15] H. Nishi *et al.*, "Monolithic integration of InP wire and SiOx waveguides on Si platform," *IEEE Photon. J.*, vol. 7, no. 5, Oct. 2015, Art. no. 4900308.

[16] G. Roelkens *et al.*, "III–V/silicon photonics for on-chip and intra-chip optical interconnects," *Laser Photon. Rev.* vol. 4, no. 6, pp. 751–779, 2010.

[17] M. Piles *et al.*, "Low-loss silicon nitride AWG demultiplexer heterogeneously integrated with hybrid III-V/silicon photodetectors," *IEEE J. Lightw. Technol.*, vol. 32, no. 4, pp. 817–823, Feb. 2014.

[18] G. Duan *et al.*, "New advances on heterogeneous integration of III–V on silicon," *IEEE J. Lightw. Technol.*, vol. 33, no. 5, pp. 976–983, Mar. 2015.

[19] K. Okazaki *et al.*, "Optical coupling between SiOxNy waveguide and Ge mesa structures for bulk-silicon photonics platform," in *Proc. IEEE Group IV Photon.*, Vancouver, BC, Canada, 2015, paper no. WP43.

[20] H. Nishi *et al.*, "Optical nonlinear ity of InP waveguide at 1550-nm band," to be submitted.

[21] W. Bogaerts *et al.*, "Compact wavelength-selective functions in silicon-on-insulator photonic wires," *IEEE J. Sel. Topics Quantum Electron.*, vol. 12, no. 6, pp. 1394–1401, Nov./Dec. 2006.

[22] T. Hiraki *et al.*, "Deuterated SiN/SiON waveguides on Si platform and their application to C-band WDM filters," *IEEE Photon. J.*, vol. 9, no. 5, Oct. 2017, Art. no. 2500207.

[23] N. P. Diamantopoulos *et al.*, "Energy-efficient 120-Gbps DMT transmission using a 1.3-μm membrane laser on Si," in *Proc. Opt. Fiber Commun. Conf. Expo.*, San Diego, CA, USA, 2018, paper no. M2D.5.

[24] N. P. Diamantopoulos *et al.*, "56-Gb/s VSB-PAM-4 over 80-km transmission using 1.55-mm EA-DFB laser and reduced-complexity nonlinear equalization," in *Proc. Eur. Conf. Opt. Commun.*, Roma, Italy, 2017, paper no. SC5.5.

[25] N. P. Diamantopoulos *et al.*, "On the complexity reduction of the 2nd-order Volterra nonlinear equalizer for IM/DD systems," *J. Lightw. Technol.*, submitted.

[26] Y. Matsui *et al.*, "55 GHz bandwidth distributed reflector laser," *J. Lightw. Technol.*, vol. 35, no. 3, pp. 397–403, Feb. 2017.

[27] OIF Technical options 400G-0.10, Fremont, CA 94538, 2015.

[28] OIF FEC 100G-0.10, Fremont, CA 94538, 2012.

Hidetaka Nishi received the B.E. and M.E. degrees in mechanical science and engineering and the Ph.D. degree in electronics and applied physics from Tokyo Institute of Technology, Tokyo, Japan, in 2005, 2007, and 2016, respectively.

In 2007, he joined NTT Microsystem Integration Laboratories, Atsugi, Japan. Since then he has been engaged in studies on photonic and plasmonic devices and integration technology of those.

He is a member of the Optical Society of America (OSA) and Japanese Society of Applied Physics (JSAP).

Takuro Fujii (M'17) was born in Kyoto, Japan, in 1986. He received the B.E. and M.E. degrees in system design engineering from Keio University, Kanagawa, Japan, in 2010 and 2012, respectively.

In 2012, he joined NTT Photonics Laboratories, Atsugi, Japan. He has been researching MOVPE growth of III–V semiconductors and the development of III–V semiconductor lasers on Si for photonic integrated circuits.

He is a member of Institute of Electronics, Information and Communication Engineers (IEICE) and the JSAP. He received the Young Scientist Presentation Award from the JSAP in 2014.

Nikolaos-Panteleimon (Pandelis) Diamantopoulos was born in Athens, Greece, in 1988. He received the B.Sc. degree from the University of Peloponnese, Greece, in 2009, the double-M.Sc. degree from Aston University, U.K. and Scuola Superiore Sant'Anna Pisa, Italy, in 2012, under the Erasmus Mundus EU program, and the Ph.D. degree in information and communications technology from Osaka University, Japan, in 2016. During 2011–2016, he was also involved in several EU-funded R&D projects at the Athens Information Technology (AIT) center, Greece.

In 2016, he joined NTT Device Technology Labs, Japan. His research interests include digital signal processing and modulation techniques for optical communications systems; space-division multiplexing; semiconductor laser design; and photonic integrated circuits and systems. He is a member of OSA.

Koji Takeda (S'06–M'10–SM'16) received the B.S., M.S., and Ph.D. degrees in electronics engineering from the University of Tokyo, Tokyo, Japan, in 2005, 2007, and 2010, respectively.

From 2008 to 2010, he received research fellowship for young scientists from Japan Society for the Promotion of Science. In 2010, he joined NTT Photonics Laboratories. His current research interests include ultralow-power optical interconnect, InP photonic integrated circuit, and photonic crystal lasers. He is a member of the IEICE and the JSAP.

He received the Best Student Paper Award from IEEE Photonics Society in 2009 and the Outstanding Student Presentation Award from JSAP in 2010.

Erina Kanno was born in Hokkaido, Japan, in 1989. She received the B.S. degree from Aoyama Gakuin University, Tokyo, Japan, in 2012, and the M.S. degree from the University of Tokyo, Tokyo, Japan, in 2014.

In 2014, she joined NTT Photonics Laboratories, Atsugi, Japan, in 2014. She has been researching ultralow-power consumption optical devices, including short-cavity lasers on Si.

Takaaki Kakitsuka (M'11) was born in Kumamoto, Japan, in 1971. He received the B.S. and M.S. degrees in physics and the Dr. Eng. degree from Kyushu University, Fukuoka, Japan, in 1994, 1996, and 2012, respectively. In 1996, he joined the NTT Optoelectronics Laboratories, Nippon Telegraph and Telephone Corporation, Kanagawa, Japan. He has been involved in research on semiconductor lasers and optical functional devices. From 2009 to 2011, he was a member of Research and Development Planning Department.

He is currently with the NTT Device Technology Laboratories, Atsugi, Japan. He is a member of the IEICE, the JSAP, and the Physical Society of Japan.

Tai Tsuchizawa was born in Tokyo, Japan, in 1961. He received the D.Sc. degree from the Department of Pure and Applied Sciences, University of Tokyo, Tokyo, Japan, in 1990. He is currently a Senior Research Engineer with NTT Microsystem Integration Laboratories, Atsugi, Japan. In NTT's laboratories, he has engaged in studies on ECR plasma and its application to the etching process for microfabrication. He is currently engaged in studies on fabrication technology for silicon-based optoelectronics devices.

Dr. Tsuchizawa is a member of the JSAP.

Hiroshi Fukuda (M'11) received the B.E. and M.E. degrees in nuclear engineering from Tohoku University, Sendai, Japan, in 1993 and 1995, respectively, and the Ph.D degree from the University of Tokyo in 2012.

In 1995, he joined the NTT Microsystem Integration Laboratories, Atsugi, Japan, where he has been engaged in research on microphotonics devices. Dr. Fukuda is a member of the JSAP and the IEICE.

Shinji Matsuo (M'95–SM'14–F'16) received the B.E. and M.E. degrees in electrical engineering from Hiroshima University in 1986 and 1988, respectively, and the Ph.D. degree in electronics and applied physics from the Tokyo Institute of Technology in 2008.

In 1988, he joined NTT Optoelectronics Laboratories, where he researched photonic functional devices using multiple quantum well pin modulators and VCSELs. In 1997, he researched optical networks using WDM technologies at NTT Network Innovation Laboratories. Since 2000, he has been researching high-speed tunable optical filters and lasers at NTT Photonics Laboratories and NTT Device Technology Laboratories.

Dr. Matsuo is a Senior Distinguished Researcher of NTT. He is a member of the JSAP and IEICE.